





CLOUDY View of the Warm Corona

Swayamtrupta Panda^{1,2} , Bożena Czerny¹ , Chris Done³, and Aya Kubota^{3,4}

¹ Center for Theoretical Physics (PAN), Al. Lotników 32/46, 02-668 Warsaw, Poland; spanda@camk.edu.pl

² Nicolaus Copernicus Astronomical Center (PAN), ul. Bartycka 18, 00-716 Warsaw, Poland

³ Department of Physics, University of Durham, South Road, Durham DH1 3LE, UK

⁴ Department of Electronic Information Systems, Shibaura Institute of Technology, 307 Fukasaku, Minuma-ku, Saitama-shi, Saitama 337-8570, Japan

Received 2019 January 9; revised 2019 March 12; accepted 2019 March 18; published 2019 April 24

Abstract

Bright active galaxies show a range of properties, but many of these properties are correlated, which has led to the concept of the quasar main sequence. We test whether our current understanding of the quasar structure allows the pattern observed in the optical plane formed by the kinematic line width of $H\beta$ and the relative importance of the Fe II optical emission to be reproduced. We performed simulations of the $H\beta$ and Fe II production using the code CLOUDY and well-justified assumptions about the broadband spectra, distance to the emission line region, and the cloud properties. We show that the presence of the warm corona is an important element of the broadband spectrum, which decreases the dependence of the relative Fe II emissivity on the Eddington ratio and allows the rare cases of particularly strong Fe II emitters to be reproduced. Results are sensitive to the adopted cloud distance, and strong Fe II emission can be obtained either by adopting strongly supersolar metallicity or a much shorter distance than traditionally obtained from reverberation mapping. We modeled in a similar way the UV plane defined by the Mg II line and Fe II UV pseudo-continuum, but here our approach is less successful, in general overproducing the Fe II strength. We found that the Fe II optical and UV emissivity depend in a different way on the turbulent velocity and metallicity, and the best extension of the model in order to cover both planes is to allow very large turbulent velocities in the broad-line region clouds.

Key words: accretion, accretion disks – galaxies: active – quasars: emission lines – radiative transfer

1. Introduction

Active galactic nuclei (AGN) are complex systems with properties dependent on the central black hole as well as on the surrounding medium. The unification picture leads to the division of sources into Type 1 and Type 2, depending on the orientation of the observer with respect to the symmetry axis (for a review, see Netzer 2015) and the sources' abilities to produce a strong jet (for a review, see Padovani et al. 2017). However, even if we concentrate on Type 1 AGNs without strong jets, where the central parts are not shielded from our view and the Doppler-boosted jet does not contribute to the broadband spectrum, we observe a broad range of nucleus properties. They show as a dispersion in the measured emission line intensities and in the kinematic width, absolute luminosities, and broadband indices.

Measurements of numerous properties in each quasar called for a search of some pattern in these properties. The essential step was made by Boroson & Green (1992) using principal component analysis. This line of research was pursued by many authors (Dultzin-Hacyan & Ruano 1996; Sulentic et al. 2000; Boroson 2002; Kuraszek et al. 2009; Marziani et al. 2014) and has led to the concept of the quasar main sequence. In its simplest version, it can be reduced to the optical plane, when only two quantities are considered: the kinematic width of the $H\beta$ line and the ratio $R_{\text{Fe II}}$ of the equivalent width (EW) of the Fe II emission in the 4434–4684 Å range to the EW of the $H\beta$ line (see, e.g., Boroson & Green 1992; Sulentic et al. 2000; Shen & Ho 2014; Marziani et al. 2018). The quasar main sequence forms a characteristic pattern in this optical plane.

In our recent paper (Panda et al. 2018a), we sought to model this quasar main sequence from a theoretical viewpoint. We wanted to see what the key drivers are behind this pattern. It has long been considered that the Eddington ratio (Shen &

Ho 2014) plays an important role, and the viewing angle was suggested as a second key parameter, although a trend with black hole mass was also noted (Shen & Ho 2014). We modeled the AGN sample assuming a range of black hole masses and Eddington ratios, ignoring the issue of viewing angle and spin, and we calculated the line widths and strengths for each source under some assumptions about the spectral energy distribution (SED) shape, broad-line region (BLR) distance, and density, metallicity, and turbulence in the BLR. Under these assumptions, we were able to locate our modeled quasars in the optical plane.

We found that although the Eddington ratio indeed plays a role in modeling the sequence, it definitely still needs to be coupled with a few other parameters. The cloud's density is important as well, and so is the effect of turbulence within the cloud. Also, the effect of metallicity has an important role here, especially in modeling these strong Fe II emitters. Solar abundances can indeed explain the low Fe II content part of the diagram, but one needs to consider a supersolar chemical composition if we aim to explain the far-right end of the main-sequence diagram. We were able to cover the optical plane quite well, although the viewing angle was not included. Nevertheless, one problem remained: we found that a simple increase in the metallicity factor allows us to cover up to 98% of the observed sample, but it is not enough to explain the most extreme Fe II emitters. So, the problem is not fully solved.

In the previous work, we modeled the SED assuming a contribution from the cold Keplerian disk and a contribution from the hot corona responsible for hard X-ray emission. However, observed AGN spectra usually contain another spectral component, observationally described as a “soft X-ray excess” (Arnaud et al. 1985). This component helps bridge the absorption gap between the UV downturn and the

soft X-ray upturn (Elvis et al. 1994; Laor et al. 1997; Richards et al. 2006). This component is particularly strong in narrow-line Seyfert 1 galaxies, but may also carry a dominant fraction of the luminosity in the SEDs of AGNs at lower Eddington ratios (Jin et al. 2012a, 2012b). Theoretically, this component is modeled as a warm corona with temperature of the order of 1 keV (Magdziarz et al. 1998; Czerny et al. 2003; Gierliński & Done 2004; Porquet et al. 2004, 2018; Petrucci et al. 2013, 2018; Middei et al. 2018, 2019), which covers part of the disk and Comptonizes disk photons. This component changes the far-UV and soft X-ray parts of the spectrum and thus can affect Fe II line production.

In this paper, we use a new complete model of the AGN SED (Kubota & Done 2018), which accounts for an outer standard disk, a hot corona, and an inner warm Comptonizing region to produce the soft X-ray excess. We test the role of the warm corona in shaping the quasar main sequence, and we aim to explain the presence of the strongest Fe II emitters.

2. Model

The SED model of Kubota & Done (2018) assumes that the accretion flow is completely radially stratified and emits as a standard disk blackbody from R_{out} to R_{warm} , as warm Comptonization from R_{warm} to R_{hot} , and eventually makes a transition to the hot corona part from R_{hot} to R_{ISCO} . We use the subset of the SED models that are a function of black hole mass, M , and the Eddington ratio only.

The simplifications of the original model are the following: the black hole spin here is fixed at $a = 0$ (nonrotating black hole). The fraction of the energy dissipated in the hot corona, $L_{\text{diss,hot}}$, is fixed at $0.02L_{\text{Edd}}$. This $L_{\text{diss,hot}}$ and $kT_{e,\text{hot}} = 100$ keV define the radius of the hot corona, $r_{\text{hot}} = 23$ for $\dot{m} = 0.05$. The radius of the warm corona is at twice the radius of the hot corona as per their simplified QSOSED version. The motivation for such an assumption is discussed in detail in Kubota & Done (2018) and shown in Figure 3 of their paper. We tested the effect of changes in $L_{\text{diss,hot}}$ on the values of $R_{\text{Fe II}}$ obtained. $R_{\text{Fe II}}$ increased for all Eddington ratios—from a meagre 1% at $\lambda_{\text{Edd}} = 1$, to almost 40% for the lowest values of Eddington ratio considered ($\lambda_{\text{Edd}} = 0.03$). Although not much is changed in the SED in the optical–UV part, a change in $L_{\text{diss,hot}}$ significantly affects the soft and hard X-ray components, enhancing the overall energy being dissipated from the coronal part affecting the higher excitation levels of Fe II, which increases the total Fe II strength.

These assumptions allow the complete SED to be obtained. The disk component is modeled as Novikov–Thorne (Novikov & Thorne 1973) blackbody spectrum that is modified by accounting for electron scattering. This has been approximated using a color–temperature-corrected blackbody spectrum. The color–temperature correction is important especially when close to the hydrogen ionization at $\sim 10^4$ K. This eventually shifts the peak of the resulting blackbody spectrum rightwards by a factor f_{col} (Kubota & Done 2018), which can be seen in Figure 1. This big blue bump shift toward higher temperatures decreases as the Eddington ratio goes down. Because the net flux remains the same, the disk component in optical–UV now has relatively lower normalization. This can be seen in Figure 1. The optical depth for the warm corona component in their model is defined by the spectral index of the Comptonization ($\Gamma_{e,\text{warm}} = 2.5$) for an electron temperature

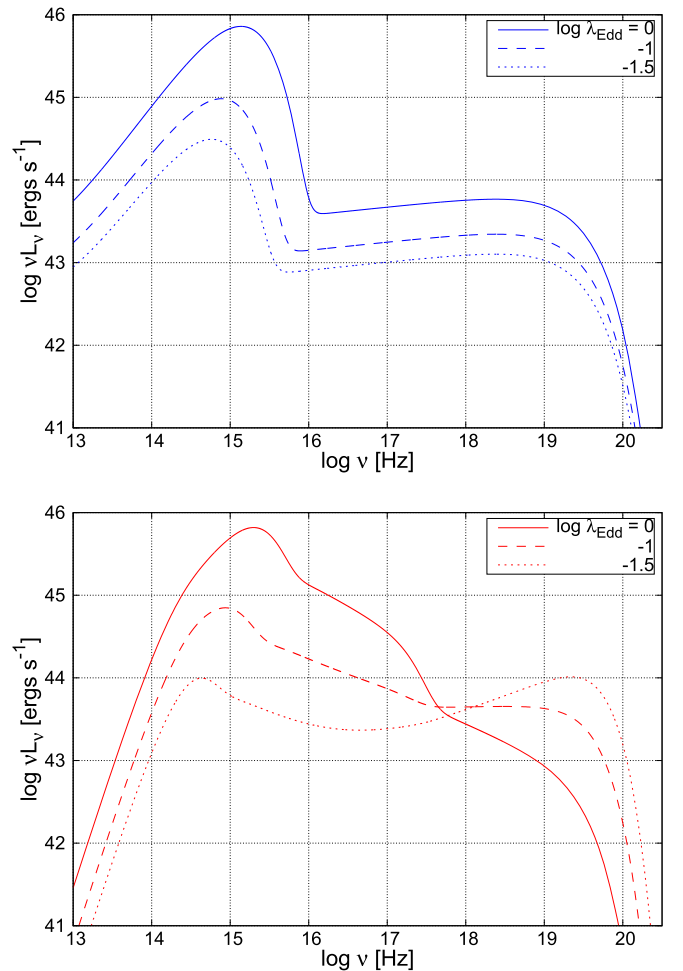


Figure 1. Comparison of the SED models from Panda et al. (2018a, P18; upper panel) and Kubota & Done (2018, WC; lower panel) for an exemplary case, $M_{\text{BH}} = 6.31 \times 10^9 M_{\odot}$. The SEDs are shown for three cases of λ_{Edd} .

$T_e = 0.2$ keV (see Table 3 in Kubota & Done 2018). Finally, the inclination angle used in our models is fixed at 45° (for Type 1 AGNs, $i \in [0^\circ, 60^\circ]$; see Marin 2014 and references therein).

Using this approach, we construct a grid of models in mass ($M_{\text{BH}} = 10^6 - 10^{10} M_{\odot}$) and in Eddington ratio ($\lambda_{\text{Edd}} = 0.03 - 1$). This range is consistent with the observed range for 545 SDSS quasars from Lusso & Risaliti (2017).

The remaining part of the modeling is done basically in the same way as in Panda et al. (2018a) although in this approach we do not need to use the UV/X-ray scaling law of Lusso & Risaliti (2017). We assume that the BLR radius is given by the Bentz et al. (2013) law (but we also discuss the possible consequences of deviating from this law in Section 3.7), we consider the same density for all clouds, we include turbulence and a range of metallicities, and the computations are done using the CLOUDY code, version 17.01 (Ferland et al. 2017).

3. Results

We use the model of emission line production to test whether our current understanding of BLR clouds allows us to reproduce the quasar main sequence pattern in the optical plane. In particular, we study the effect of the warm corona on the BLR using the SEDs from Kubota & Done (2018). We

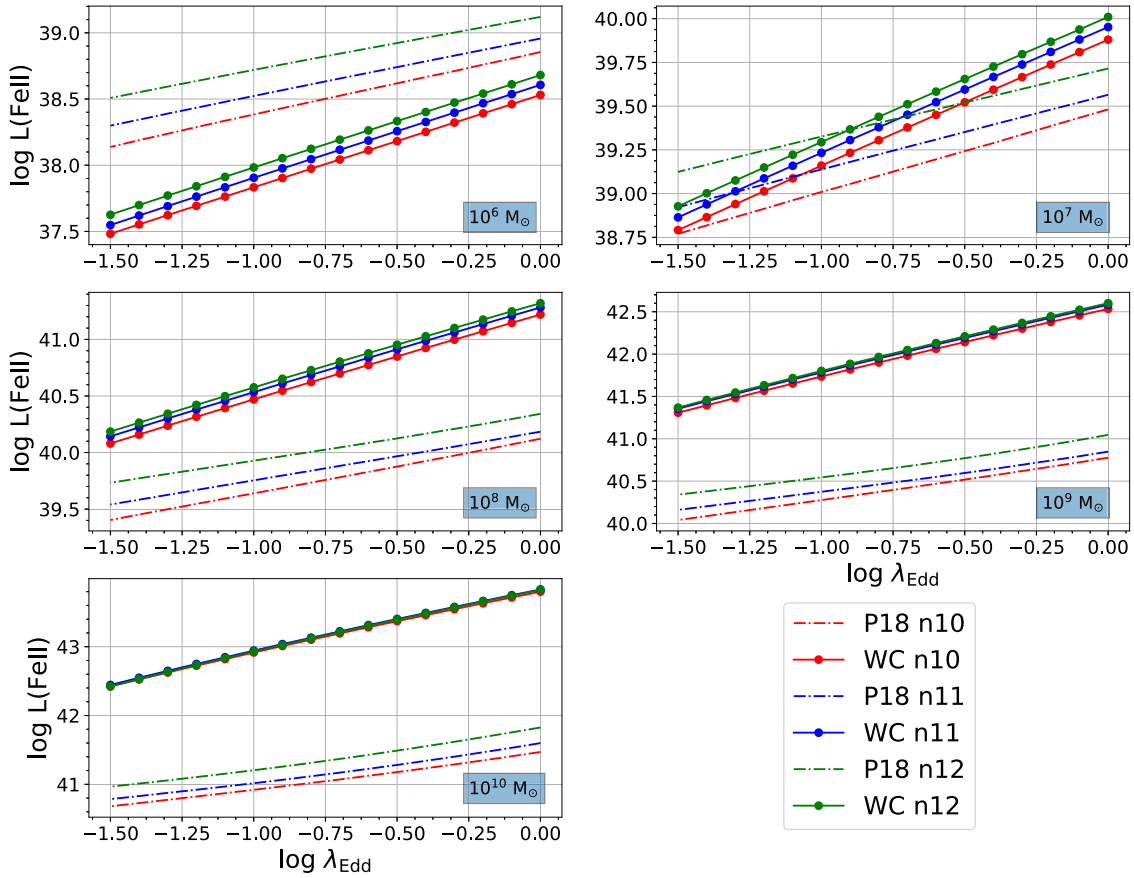


Figure 2. Optical Fe II (integrated) line luminosities vs. λ_{Edd} for $M_{\text{BH}} = 10^6$ – $10^{10} M_{\odot}$ in two models: P18 and WC, assuming no turbulence and with solar abundances.

compare the results to those obtained by Panda et al. (2018a), where such a component was not included.

3.1. Comparison of the Two SED Models

In Figure 1, we show the distinctive change in the SED shape between the two models—the warm corona (hereafter WC) and the two-component standard model (Panda et al. 2018a; hereafter P18). Here we consider the spectra (for an exemplary black hole mass $M_{\text{BH}} = 6.31 \times 10^9 M_{\odot}$) as a function of Eddington ratio (at $\lambda_{\text{Edd}} = 0.03, 0.1$, and 1). We can clearly see the warm corona component standing out in the case of the Eddington limit, and its effect lessens with the decrease in Eddington ratio. The effect of the color–temperature correction in the WC models can also be seen clearly (the disk component is shifted toward higher frequencies) as opposed to the P18 models where this effect was not accounted for.

3.2. The Effect of the Warm Corona on Fe II Production

In P18, we found that Fe II production was increasing with the Eddington ratio. We thus first check whether this trend is preserved when the presence of the warm corona is taken into account—decreasing the Eddington ratio yielded an increase in the net optical Fe II strength.

In Figure 2, we plot the integrated Fe II (from 4434 to 4684 Å, according to the Boroson & Green 1992 prescription, which refers to the blue part of the Fe II contamination lying to the left of the $H\beta$ emission line). Models are computed for three

values of cloud densities i.e., $\log n_{\text{H}}$ (in cm^{-3}) = 10, 11, and 12, and for a specific value of the hydrogen column density ($N_{\text{H}} = 10^{24} \text{cm}^{-2}$). Here, we show the trends for five cases of black hole masses ($M_{\text{BH}} = 10^6 - 10^{10} M_{\odot}$) that cover the full range of the models. We see that the Fe II line luminosity rises with the Eddington ratio as before, for all values of the black hole mass. However, this rise is now generally steeper than that in previous P18 models. In these computations, the turbulence was not included in the models, and solar abundance was assumed.

In Figure 3, we show similar plots for the $H\beta$ line luminosities. Again, the line luminosity rises with the Eddington ratio both in the P18 model and in the present WC model. The rise again is steeper if the contribution from the warm corona is included.

The results become more interesting when we finally plot the ratio of Fe II to $H\beta$ (see Figure 4). Without the warm corona, this value (i.e., the parameter $R_{\text{Fe II}}$) showed a declining trend with increasing Eddington ratio. But with the new results for the warm corona model, the previous trend between $R_{\text{Fe II}}$ and the Eddington ratio disappears. The ratio $R_{\text{Fe II}}$ slightly depends on the black hole mass, but it is constant for a given mass and for all values of the local cloud density. The values themselves are almost universal, with only a slight trend with the cloud density: higher density leads to a slightly more efficient Fe II production in comparison to $H\beta$.

This will have important consequences on the trends observed in the optical plane. It was frequently argued that high values of $R_{\text{Fe II}}$ correspond to high values of the Eddington

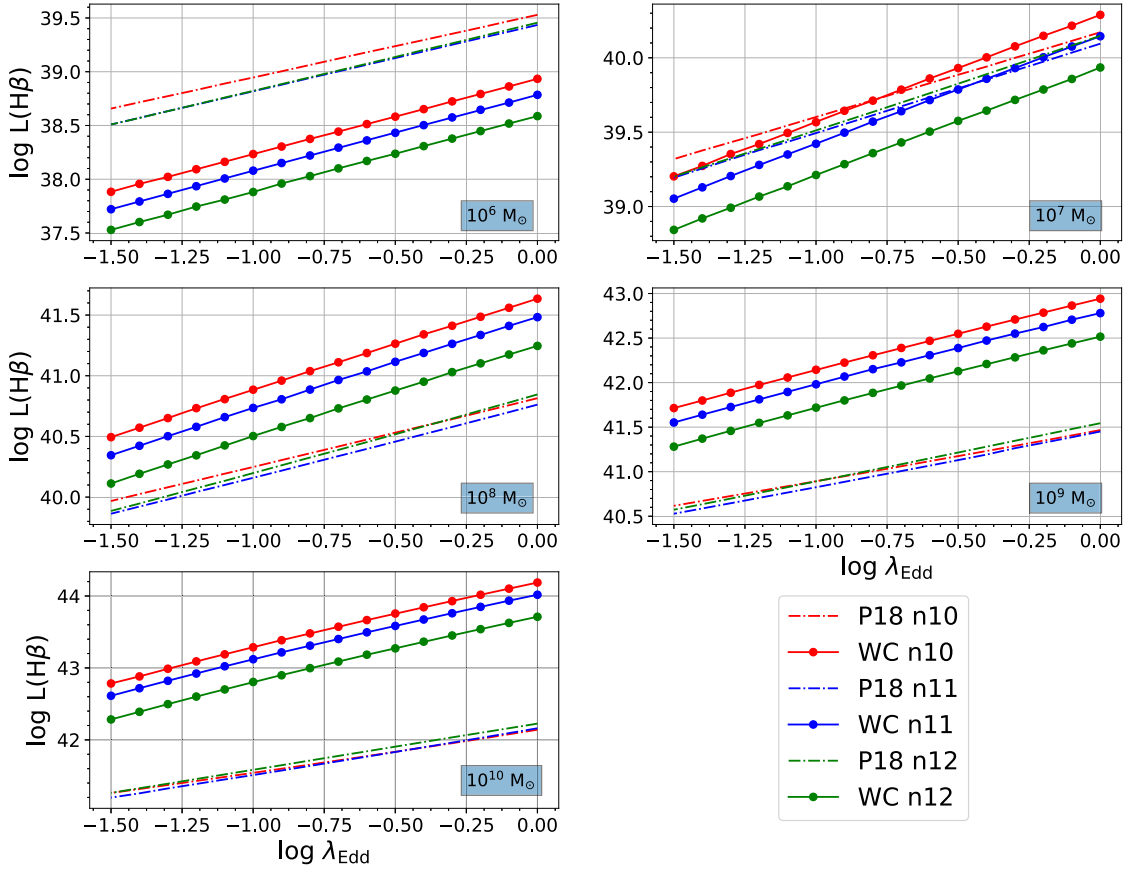


Figure 3. $H\beta$ line luminosities vs. λ_{Edd} for $M_{\text{BH}} = 10^6\text{--}10^{10} M_{\odot}$ in two models: P18 and WC, assuming no turbulence and with solar abundances.

ratio (e.g., Marziani et al. 2018). On the other hand, sources identified by the Super-Eddington Accreting Massive Black Holes (SEAMBH) project as high-Eddington-ratio sources (Du et al. 2014, 2016b, 2018) show quite a broad range of values of $R_{\text{Fe II}}$, from 0.5 to 2 (see Figure 3 in Czerny et al. 2018a). From an observational point of view, the issue is quite open.

The values of $R_{\text{Fe II}}$ are now somewhat higher than those obtained in P18, particularly in the case of high Eddington ratio, which is promising if we aim to cover well the whole optical plane occupied by the observational points. However, here the discussion did not include the option of higher metallicity and the effect of turbulence. This we address in the next section.

3.3. The Effect of the Warm Corona on the Quasar Optical Plane

Finally, we aim to reproduce statistically the coverage of the optical plane with our modeled sources. We model the whole range of masses and accretion rates, as described in Section 2. However, the observational construction of the optical plane is biased by the choice of only high-Eddington-ratio sources in the case of small black hole mass, due to the flux limits in the quasar sample. We showed in P18 that the quasars in the Shen et al. (2011) catalog populating the $\log M_{\text{BH}}\text{--}\log \lambda_{\text{Edd}}$ plane are limited by the relation $\log(\lambda_{\text{Edd}}) = -1.05 \log(M_{\text{BH}}) + 7.15$. We show this in Figure 5, and in a future study we will take into consideration mostly models that populate the white part of the diagram.

Figures 6 and 7 show the full scale of the modeled sequence with the warm corona model. In Figure 6, the $v_{\text{FWHM}}\text{--}R_{\text{Fe II}}$

diagram is shown for varying cloud densities ($\log n_{\text{H}}$ (in cm^{-3}) = 10, 11, and 12), without the effect of turbulence. The three panels show the effect of changing abundances ($Z = Z_{\odot}$, $3Z_{\odot}$, and $10Z_{\odot}$). The plots show the full sequence ($M_{\text{BH}} = 10^6\text{--}10^{10} M_{\odot}$; λ_{Edd} from $\sim 3\%$ up to the Eddington limit) and the sequence constrained by the detection limit given in Figure 5. In our analysis, we derive the FWHM value from the BLR radius and black hole mass assuming the value of the virial factor to be 1 (see Equation (1) in P18) for simplicity; Shen & Ho (2014) and Mejía-Restrepo et al. (2018) showed strong coupling between the virial factor and the line width.

An increase of the cloud density clearly leads to an increase in the Fe II strengths (overall rise a factor of ~ 1.65 going from n_{H} (in cm^{-3}) = 10^{10} to 10^{11} , and a factor of ~ 3.1 going from n_{H} (in cm^{-3}) = 10^{10} to 10^{12}). However, the predicted increase of the Fe II strength is correlated with the $H\beta$ line widths: relatively stronger Fe II emission is expected for broader line galaxies. This is rather unexpected as there are not many Seyfert 1 galaxies detected with such high Fe II strengths. This may point toward a dependence between the cloud density and the kinematic line width, which can be achieved through an intrinsic dependence between cloud density and the Eddington ratio. Arguments for such coupling can be found, for example, in Adhikari et al. (2016), where high densities were required to form Lorentzian line profiles without a clear gap between the BLR and narrow-line region, a characteristic of NLS1.

As we increase the overall cloud abundances (from solar to 10 times solar), we do obtain Fe II strengths that are comparable to those obtained for “strong” NLS1 sources (occupying the rightward tail region in the Shen & Ho 2014 quasar main-

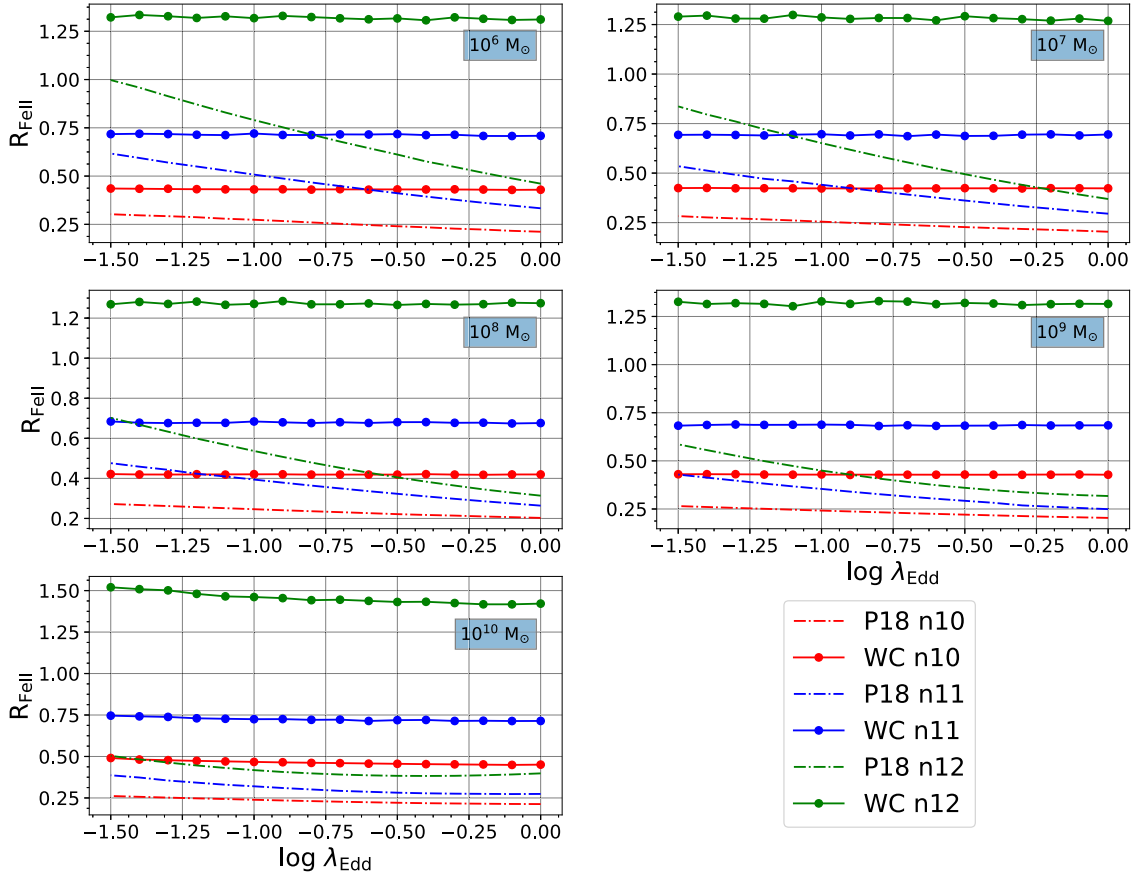


Figure 4. $R_{\text{Fe II}}$ vs. λ_{Edd} for $M_{\text{BH}} = 10^6$ – $10^{10} M_{\odot}$ in the P18 and WC models. Almost no dependence on Eddington ratio is seen in the model with warm corona.

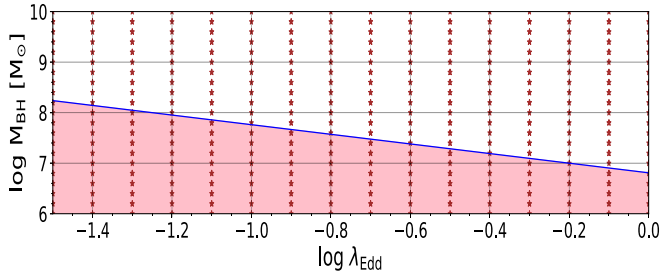


Figure 5. The parameter space for the construction of the optical plane: the pink shaded region represents the unobserved region in the Shen et al. (2011) quasar sample. The stars represent the grid points used in the computations.

sequence diagram). As can be seen, in the limited sequence, there are a significant number of expected NLS1s that are excluded. There is an overall rise in $R_{\text{Fe II}}$ from ~ 0.42 ($n_{\text{H}} = 10^{10} \text{ cm}^{-3}$; $Z = Z_{\odot}$) to ~ 4.5 ($n_{\text{H}} = 10^{12} \text{ cm}^{-3}$; $Z = 10 Z_{\odot}$). These values for the narrower broad H β cases range from ≤ 0.44 ($n_{\text{H}} = 10^{10} \text{ cm}^{-3}$; $Z = Z_{\odot}$) to ≤ 3.45 ($n_{\text{H}} = 10^{12} \text{ cm}^{-3}$; $Z = 10 Z_{\odot}$).

Another interesting result is that none of the modeled values for the FWHM of the H β line drops below the limit of 2000 km s^{-1} , so formally our current model does not cover the NLS1. Our black hole mass range includes small values, as we start from $10^6 M_{\odot}$. In the Shen & Ho (2014) diagram, there are sources with FWHM below 1500 km s^{-1} , although not too many. The absence of narrow-line objects in our model is likely related to two effects—assuming the value of the virial factor to be 1 (see Equation (1) in P18) for simplicity while Shen & Ho

(2014) and Mejía-Restrepo et al. (2018) show a strong coupling between the virial factor and the line width. Thus, the virial factor for narrower lines should be considerably higher, up to a factor of a few, and in this way we would obtain an FWHM from the model that is smaller by the same factor. In the present study, we decided not to use a more complex prescription for the line width versus black hole mass relation in order not to complicate the picture too much. The second plausible reason is that we do not include in the present study the problem of the viewing angle range, and the viewing angle can have some effect on the measured line width (Shen & Ho 2014; Sun et al. 2018).

In Figure 7, a similar $v_{\text{FWHM}}-R_{\text{Fe II}}$ diagram is shown, but with the cloud density kept constant at high value ($n_{\text{H}} = 10^{12} \text{ cm}^{-3}$) and the turbulence within the cloud is changing ($v_{\text{turb}} = 0, 10$ and 20 km s^{-1}). Similar to Figure 6, three cases of abundances are considered. The panels clearly show the effect of coupling between the high density within the clouds and a non-negligible microturbulence. We observe an increase in the overall Fe II strengths (starting from ~ 1.3 for $v_{\text{turb}} = 0 \text{ km s}^{-1}$, $Z = Z_{\odot}$; to almost a factor of 4.5 increase for the case with $v_{\text{turb}} = 20 \text{ km s}^{-1}$, $Z = 10 Z_{\odot}$). However, unlike Figure 6, the almost monotonic behavior in the $v_{\text{FWHM}}-R_{\text{Fe II}}$ plane is gone. Increasing the turbulence to a finite value (10 – 20 km s^{-1}), even for the limited sequence (see Figure 7), shows a marked increase in the number of low-FWHM sources, although a large number of low-FWHM sources get excluded again with this constraint. As in our findings in P18, the case with 10 km s^{-1} usually gives the highest Fe II strength (compared to the other two cases). Further

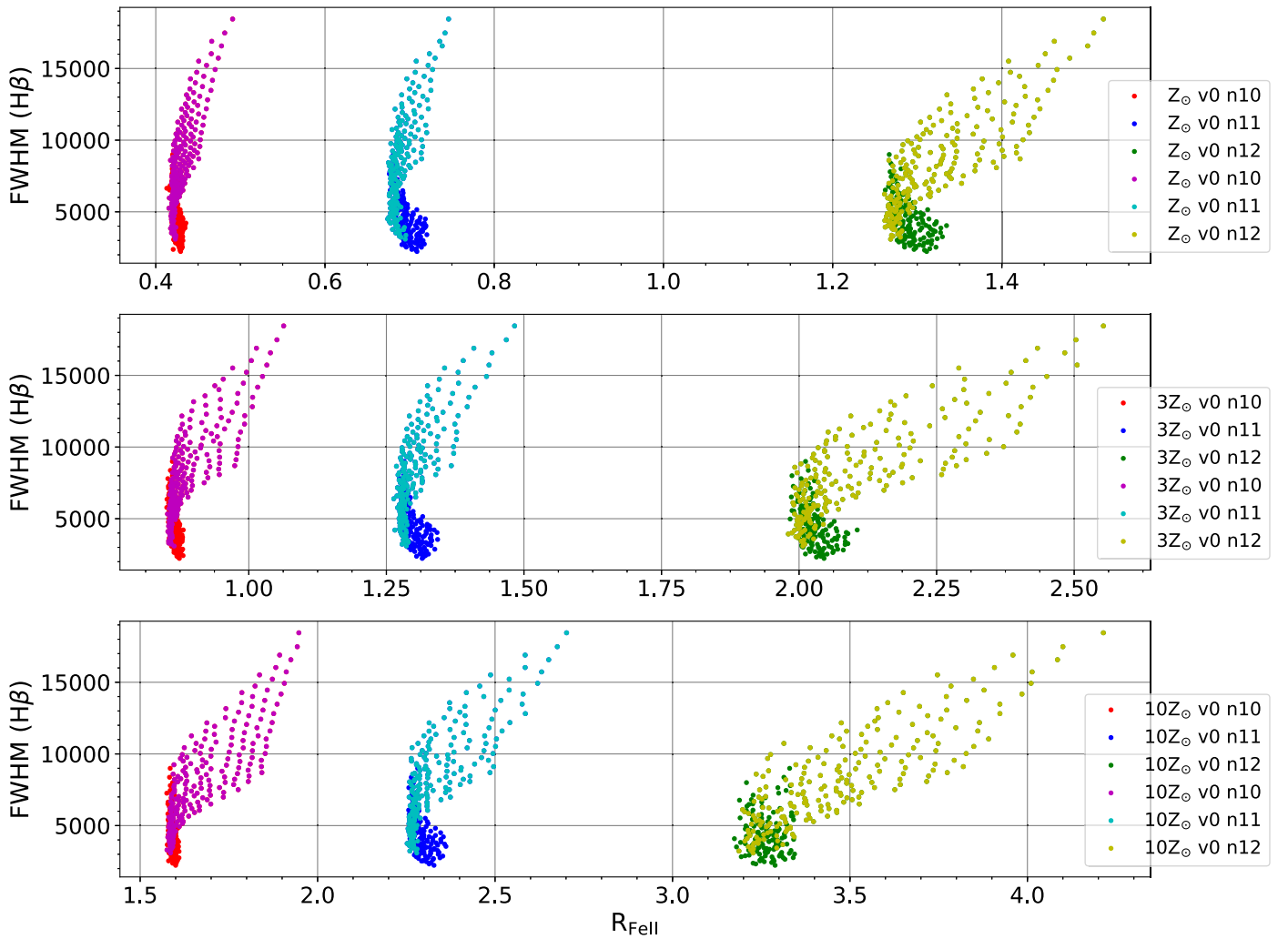


Figure 6. The coverage of the optical plane for a range of abundances (1, 3, and 10 times solar) and changing cloud densities ($\log n_{\text{H}}$ (in cm^{-3}) = 10, 11, and 12) at constant turbulent velocity (0 km s^{-1}). Two cases are shown for each value of the parameter: lighter colors (magenta, light blue, and light green) represent the limited parameter range shown in Figure 5, and the remaining objects in the whole mass–Eddington ratio range are shown in darker color (red, blue, and green).

increase of the microturbulence leads in general to a decline in the strengths. However, increasing the abundances makes the strengths obtained comparable in the $v_{\text{turb}} = 10 \text{ km s}^{-1}$ and 20 km s^{-1} cases—for the $Z = 10 Z_{\odot}$ case, the higher turbulence case actually leads compared to the 10 km s^{-1} . The small region at the higher $R_{\text{Fe II}}$ in the last panel ($Z = 10 Z_{\odot}$; $v_{\text{turb}} = 10 \text{ km s}^{-1}$) is probably the result of some thermal instabilities in the models and the corresponding discontinuous change in the cloud structure as the grids of the parameters in the models are homogeneous. This blob is no longer seen when the observational cut (based on Figure 5) to the parameter space is added.

To cover well the whole observed optical plane, we need a whole range of black hole masses, Eddington ratios, cloud densities, metallicities, and turbulent velocity. As in P18, the average sources in the Shen et al. (2011) catalog are modeled well with just solar abundance and a range of densities. But now, if some turbulence, high cloud density, and high metallicity are allowed, our model also covers the region of very high values of the $R_{\text{Fe II}}$ parameter, up to ~ 5 – 6 , so now even extreme Fe II emitters can be reproduced. This was not achieved in P18, so the presence of the warm corona brought

our model closer to the observed properties of the quasar sample.

3.4. Comparison of the Model with the Data Coverage of the Optical Plane

Previous sections show that with the present model, we can represent even extreme Fe II emitters, but proper coverage of the optical plane requires also not populating the part of the plane when real objects are not seen. With this aim, we selected the optimum but representative parameter examples and plotted them against the data points from the Shen & Ho (2014) catalog, as we did in P18. The results are shown in Figure 8. Lines show only representative cases, and the spaces between the lines can be easily filled by models at parameter values intermediate to those presented in the plot.

This optimum coverage requires the use of only low-density, low-metallicity, and low-turbulence-velocity clouds for low Eddington ratios, and a subsequent increase in the metallicity, density, and turbulence with the Eddington ratio. The lowest density, metallicity, and turbulence allow objects located at the extreme left of the diagram to be recovered. With higher density, low Eddington ratio clouds, we would overpopulate the part of the diagram with high values of the FWHM at high

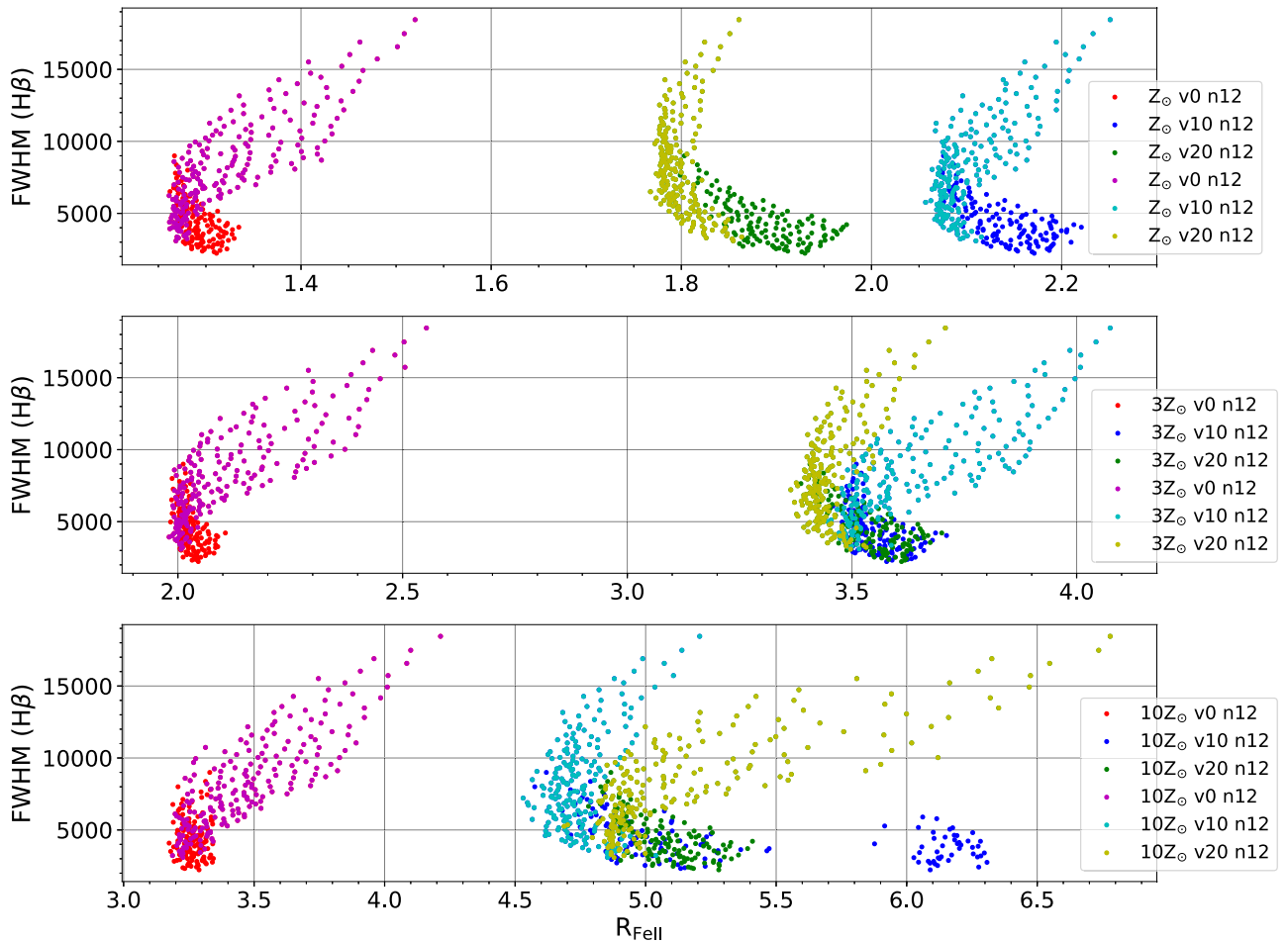


Figure 7. The coverage of the optical plane for a range of abundances (1, 3, and 10 times solar) and changing turbulent velocities (0, 10, and 20 km s^{-1}) at constant cloud density ($n_{\text{H}} = 10^{12} \text{ cm}^{-3}$). Two cases are color-coded as in Figure 6.

values of $R_{\text{Fe II}}$, where real objects are rare. This is related to the fact that most effects (like changing metallicity or turbulent velocity; see Figure 7) only weakly affect the line width.

This selection is not entirely unique, but it allows the observed quasar main sequence to be better reproduced. It also takes us back to some correlation between the metallicity and the Eddington ratio. While in Figure 4 we showed that $R_{\text{Fe II}}$ does not depend on the Eddington ratio λ_{Edd} , the dependence now reappears, caused by the coupling of λ_{Edd} , cloud density, and metallicity. Our model does not predict such coupling because for us, all three quantities are free parameters. We cannot study quantitatively the coupling, as at that stage perhaps other couplings can also be suggested, and they would shrink the range of FWHM and λ_{Edd} now covered by the model.

3.5. Quasar Main Sequence in the UV Plane

The quasar main sequence is customarily studied in the optical plane, but a similar study can be done in the UV plane. In this case, the Mg II line at 2800 Å has to be used instead of H β , and the Fe II optical emission has to be replaced with equally intense UV emission. Mg II and H β both belong to low-ionization lines, as classified by Collin-Souffrin et al. (1988), and thus should behave similarly. In Śniegowska et al. (2018), we showed that the UV plane of the quasar main sequence based on the Mg II line and Fe II (in the UV) emission indeed

looks similar to the optical plane based on H β line and Fe II (in the optical).

We thus use our model to test whether it can also reproduce the quasar main sequence in the UV plane. To do so, we used the warm corona models and the same assumptions about the location of the BLR and cloud parameters, and with the use of the code CLOUDY, we perform computations of the line intensities, constructing a similar main-sequence diagram using the integrated Fe II emission strength in the UV. The range of Fe II emission in the UV is considered to be within 2900–3050 Å (the redder side of the Fe II contamination in Figure 5 of Kovačević-Dojčinović & Popović 2015). This Fe II strength is derived by normalizing the integrated Fe II emission with the Mg II emission. This selection of the wavelength range is considered because at shorter wavelengths it is difficult to disentangle the blue wing of Mg II from Fe II contribution.

Similar to the optical plane relations, we now show the predicted dependence of the FWHM of the Mg II line on the parameter R_{Fe} (UV) measuring the relative strength of Mg II and UV Fe II (see Figure 9). The results again depend on the adopted density, turbulence, and metallicity, but the trends are not the same as in the case of the optical plane. There is, for example, a large overlap between the plots for different densities or turbulent velocities, if solar metallicity is assumed. The non-monotonic behavior in the top panels of Figure 9 nearly goes away as the abundances are increased (from $Z = Z_{\odot}$ to $Z = 10 Z_{\odot}$). But, similar to the case of the optical

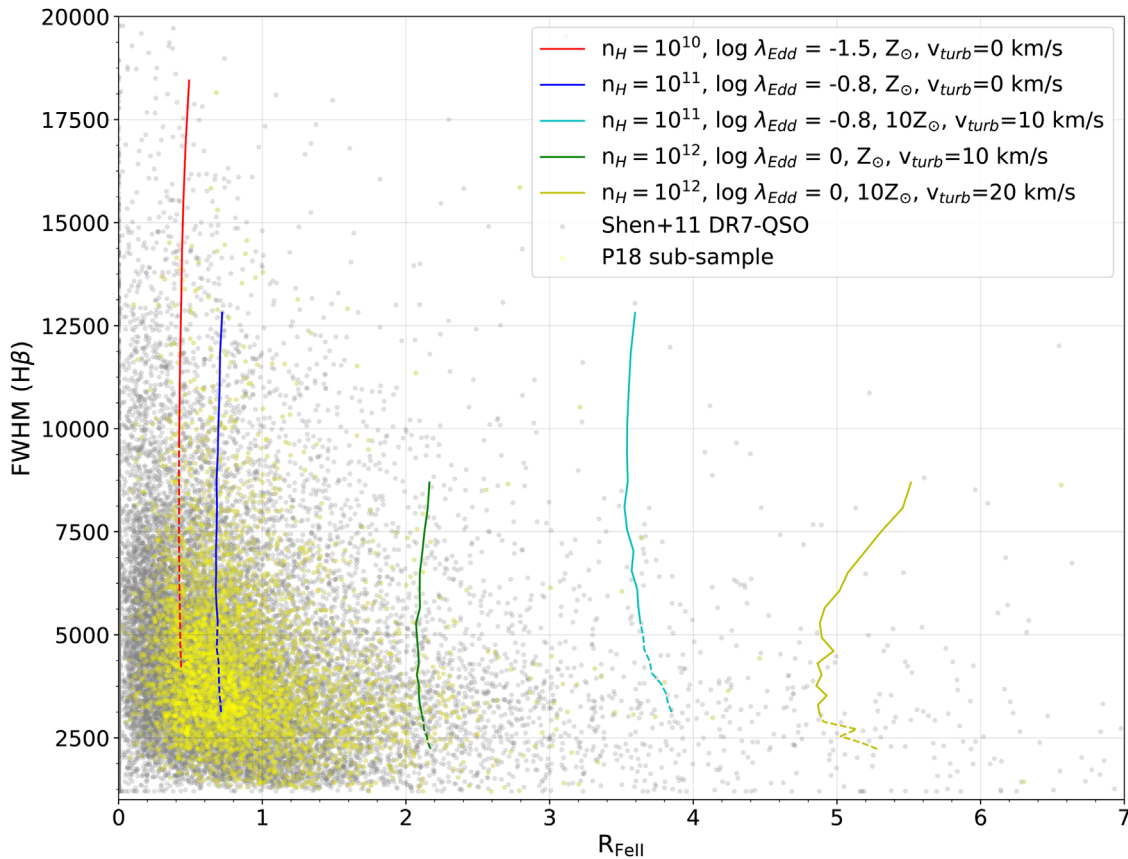


Figure 8. The coverage of the optical plane is shown with a broad range of parameters: mean cloud density ($\log n_H$ (in cm^{-3}) = 10–12), solar to 10 times solar abundances, 0–20 km s^{-1} microturbulence, for a single-density cloud at a high column density ($\log N_H$ (in cm^{-2}) = 24). The observational data points from the Shen et al. (2011) DR7-QSO catalog, and a cleaner subset from Panda et al. (2018b), are plotted to show the coverage of the modeled sequence.

plane, Fe II emissivity is strongly enhanced when metallicity higher than solar is introduced, and when BLR clouds have higher densities.

The most significant difference between the optical and the UV plane is in fact in the dependence on the turbulence velocity. Now, an increase of the turbulence from 0 to 20 km s^{-1} results in a significant reduction of the Fe II emissivity.

The range of the FWHM is the same as before because we did not introduce any correction for the location of the peak of the Mg II emission. Observationally, there are some indications that Mg II is located somewhat farther than H β as the Mg II lines are narrower by a factor of 0.81, as shown in Wang et al. (2009), but the difference is not large, and it was not included in the present study.

We now overplot a few sequences of selected models on top of the observational data. Data points and models are shown in Figure 10. The data points, as in Śniegowska et al. (2018), come from the QSFIT catalog of Calderone et al. (2017).

Observationally, the UV quasar plane suggests a somewhat narrower range of the FWHM than the optical plane, up to 9000 km s^{-1} instead of 12,000 km s^{-1} in the optical plane for the same sample (Śniegowska et al. 2018). The observed values of $R_{\text{Fe II}}$ (UV) are centered around ~ 5 , and in extreme cases extend up to 12, but in Śniegowska et al. (2018), we used a different wavelength range to measure the Fe II contribution (from 1250 to 3090 Å), which is much broader than in the present paper (2900–3050 Å), so a direct comparison is not possible. We thus replot the data points from Śniegowska et al. (2018), rescaling the values of $R_{\text{Fe II}}$ (UV) by a factor of 0.085

obtained as a ratio between EW(Fe II) in the wavelength range used by QSFIT (Calderone et al. 2017) and the wavelength range used in the current study. This was done for the Fe II template of Vestergaard & Wilkes (2001) adopted by QSFIT.

We see from Figure 10 that the parameter range adjusted to fit the optical plane does not reproduce the UV plane well if we limit ourselves to the turbulent velocities between 0 and 20 km s^{-1} , as we did when modeling the optical plane. The predicted Fe II emissivities are much higher than seen in the data, with $R_{\text{Fe II}}$ (UV) mostly above 0.4 while the data points concentrate at ~ 0.2 . We may argue that the emission comes from a different region, but we prefer to check first if indeed it is necessary, and we reconsider the adopted parameter range for the turbulence.

In P18, we studied a much broader range of turbulent velocities, and we noticed that the dependence is not monotonic (see Figure 5 in P18). The trend depends on the density, but basically, for the optical Fe II emission, the emissivity first rises with the turbulent velocity, and for values above 20 km s^{-1} , it decreases again, so the case of high turbulence velocity is actually similar to the very low-turbulence velocity. Thus, if we dramatically broaden the range of turbulent velocities in Figure 8 (optical plane with data points), this coverage will not change. However, in the case of the UV plane, further increase of the turbulent velocity leads to further reduction of the Fe II emissivity, and with values of order of 100 km s^{-1} , we can now reach the center of the object population in the UV plane, and thus cover approximately the UV plane as well (see

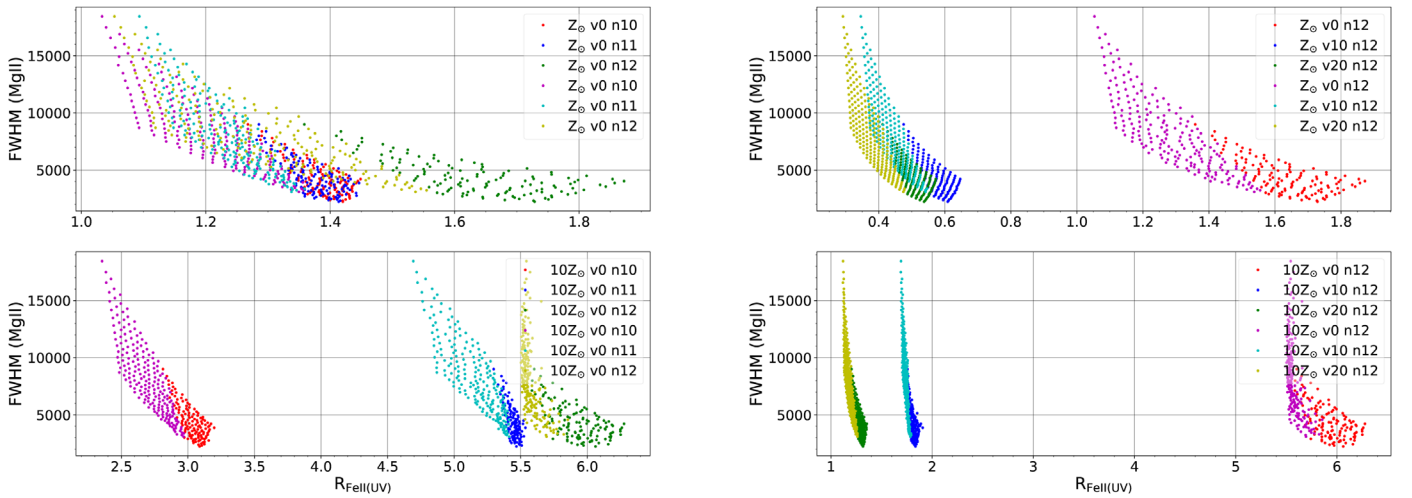


Figure 9. The coverage of the UV plane for two extreme cases of abundances (top panels: at solar; and bottom panels: 10 times solar). Left panels: changing cloud density ($n_{\text{H}} = 10^{10}, 10^{11},$ and 10^{12} cm^{-3}) at zero turbulent velocity. Right panels: changing turbulent velocities (0, 10, and 20 km s^{-1}) at constant cloud density ($n_{\text{H}} = 10^{12} \text{ cm}^{-3}$). The two cases are color-coded as in Figure 6.

the line most to the left in Figure 10, still within the scheme of a single-density, single-distance model).

3.6. Comparing Fe II Strength in the Optical and UV

We compare the Fe II strength obtained in the optical (integrated Fe II EW within $4434\text{--}4684 \text{ \AA}$ normalized by the broad $\text{H}\beta$ EW) and UV (integrated Fe II EW within $2900\text{--}3050 \text{ \AA}$ normalized by the broad Mg II EW). Figure 11 shows the dependence between $R_{\text{Fe II}}$ (optical) and $R_{\text{Fe II}}$ (UV) for the WC model at solar abundances for three cases of cloud densities ($\log n_{\text{H}}$ (in cm^{-3}) = 10, 11, and 12) without turbulence. The exact values of the parameters depend predominantly on the set range of wavelength, but the plot is an interesting illustration of the trends with changing density. The two values are not proportional, as we might expect. In some parameter range, the relation predicts two distinct values of $R_{\text{Fe II}}$ (UV) strengths for a given $R_{\text{Fe II}}$ (optical). Therefore, on the basis of the model, we would not expect a strong correlation between Fe II optical and UV emission, and indeed such a correlation is not seen in the observational data (Kovačević-Dojčinović & Popović 2015).

3.7. R_{BLR} Scaling

Recent time-lag studies (Grier et al. 2017) show that the BLR size could be lower by a factor of 15 than the predicted sizes from the radius–luminosity relation (Bentz et al. 2013). In P18, we tested this effect of BLR clouds being closer than predicted by Bentz et al. (2013), which gave higher Fe II strengths. This can indeed be true for many of the quasars that have high Fe II contamination in their spectra. We have tried to incorporate this into the WC models. We tried to scale the BLR sizes to a lower limit of 15 times smaller going up to $\sqrt{15}$ times smaller than the original BLR sizes obtained from the Bentz et al. (2013) relation. In Figure 12, we show the scaling of the $v_{\text{FWHM}}\text{--}R_{\text{Fe II}}$ relation when the radius of the BLR clouds is reduced by these factors. Like in the previous plots, we show both the full sequence and the limited range from observations. We use a cloud density of n_{H} (in cm^{-3}) = 10^{12} at solar abundances for two cases of turbulence ($v_{\text{turb}} = 0$ and 10 km s^{-1}). As expected, the spread in the optical plane

monotonically increases as the size gets smaller. Here, we did not change the corresponding FWHM, because in this case the Bentz et al. (2013) relation does not apply. It may seem that lines should become broader as we move the BLR closer in but actually the change can be equally well absorbed by the virial factor, in general present in the mass–radius–velocity relation. We would need another method to locate the BLR, and to determine the line width, for a given black hole mass. For example, Czerny et al. (2018b) suggested returning to the size–luminosity relation based on bolometric flux, while Du et al. (2016a) argued that with the inclusion of the high-Eddington sources, the scatter in the $R\text{--}L$ relation shows a clear departure from the one-to-one relation in Bentz et al. (2013). Discrimination between the two options is beyond the scope of the present paper as these short lags come from a relatively short campaign and need confirmation. However, a strong trend of Fe II increase is interesting.

4. Discussions

The aim of the project was to test our understanding of the quasar main sequence by attempting to reproduce the distribution of the observational points in the optical plane with the theoretical model. The model assumed a grid of black hole masses and Eddington ratios. The distance to the BLR was assumed using the radius–luminosity relation of Bentz et al. (2013), which gave us the line width, and the emission line fluxes were calculated using the code CLOUDY v17.01 (Ferland et al. 2017), for a range of densities, metallicities, and turbulent velocities. In P18, we were able to cover most of the region apart from the strongest Fe II emitters. In the present work, we cover this region as well (see Figure 8), because we now include the warm corona in modeling the object SED.

The presence of the warm corona significantly affects the Fe II and $\text{H}\beta$ emissivity. Without the warm corona, the line ratio $R_{\text{Fe II}}$ was sensitive to the Eddington ratio, while with the warm corona, this dependence disappeared. This means that high-Eddington-ratio sources can be found between strong Fe II emitters as well as between weak Fe II emitters, consistent with the classical concept of NLS1 as high-Eddington-ratio sources, independently from Fe II strengths. This would need further

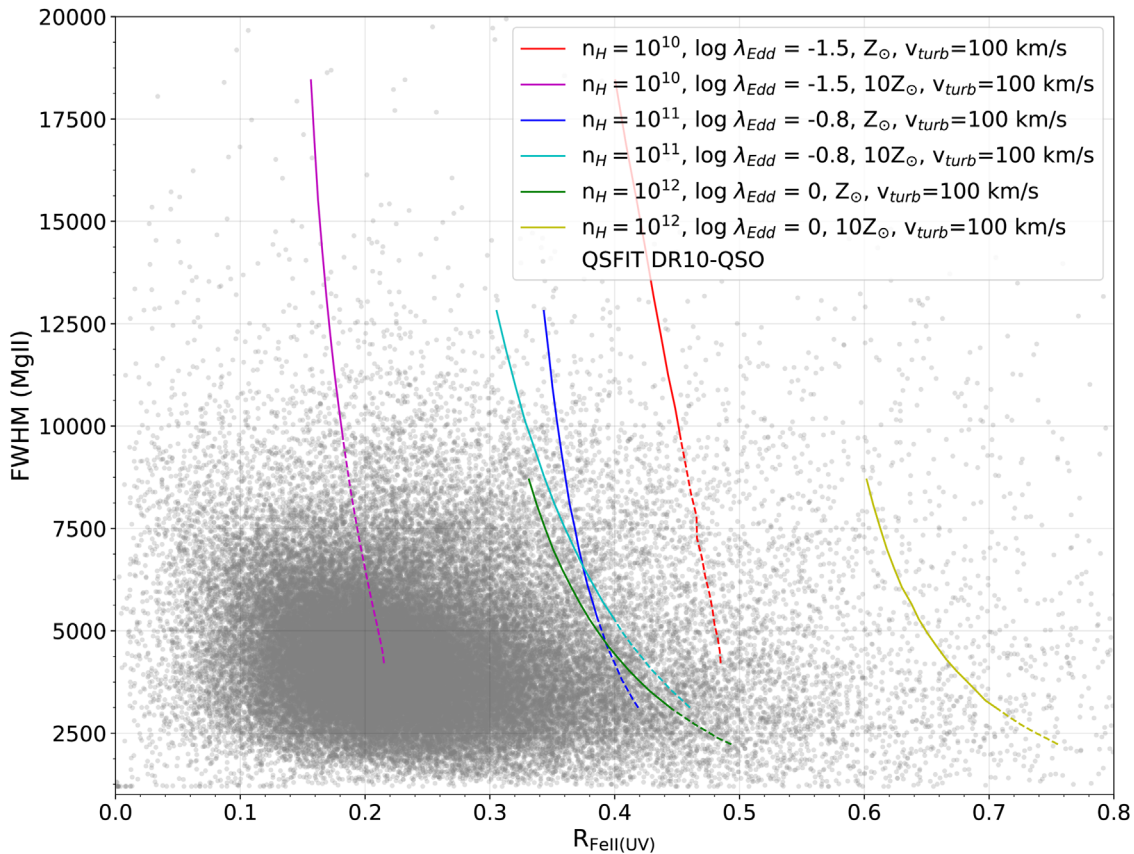


Figure 10. The coverage of the UV plane is shown with a broad range of parameters: mean cloud density ($\log n_H$ (in cm^{-3}) = 10–12), solar to 10 times solar abundances, at 100 km s^{-1} microturbulence, for a single-density cloud at a high column density ($\log N_H$ (in cm^{-2}) = 24). The observational data points from the QSFIT catalog (Calderone et al. 2017) are plotted to show the coverage of the modeled sequence.

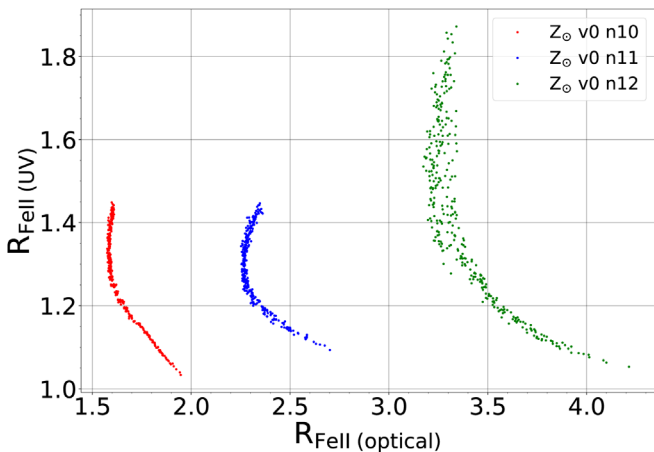


Figure 11. Fe II strength in optical vs. UV. The optical Fe II range considered is 4434–4684 Å, while in the UV it is 2900–3050 Å. The integrated Fe II emission is then normalized by broad H β and Mg II, respectively, to get the corresponding Fe II strengths. The plots shown are for three cases of mean cloud density (10^{10} , 10^{11} , and 10^{12} cm^{-3}) at zero turbulence and solar metallicity.

support from individual modeling of sources located in the lower left corner of the optical plane.

Good coverage of the whole plane requires a range of cloud densities, turbulence, and metallicities, because high-density, high-metallicity clouds are more efficient Fe II emitters. However, a simple increase of the metallicity led only to the displacement of the modeled sequence rightward, which was

enough to cover the region of high Fe II emitters at low values of FWHM but at the same time overpredicted the number of high FWHM emitters at that $R_{\text{Fe II}}$ location. In order to cover the optical plane more precisely instead of too broadly, we need a coupling among these quantities. We see from the trends presented in Figure 6 that, for a fixed density, the highest values of the FWHM correspond to the highest black hole masses and the lowest Eddington ratios. If we postulate that density and/or metallicity increases with the Eddington ratio or decreases with the black hole mass, then we could reproduce the coverage of the optical plane more precisely, populating the right part of the diagram mostly with high-Eddington, low-mass sources. Such a trend has been noticed already (for both Eddington ratio and black hole mass) by Shen & Ho (2014). However, the procedure is not unique; for example, the rise in density gives a qualitatively similar effect to the rise of metallicity so we do not attempt to perform this exercise quantitatively.

The current model still has problems with reproducing the lowest values of the line widths. This may be due to the use of a fixed virial factor of 1 connecting the black hole mass, BLR distance, and the FWHM of the lines. If we adopt, for example, a virial factor of 1.3, as recently derived by the GRAVITY Collaboration et al. (2018) for a spatially resolved BLR in 3C 273, the line width values become smaller by a factor of 14%. However, the virial factor likely depends on the FWHM itself, as argued by Mejía-Restrepo et al. (2018), and the suggested virial factor range implies a possibility of line widths smaller even by a factor 2. Additionally, the problem of the line width

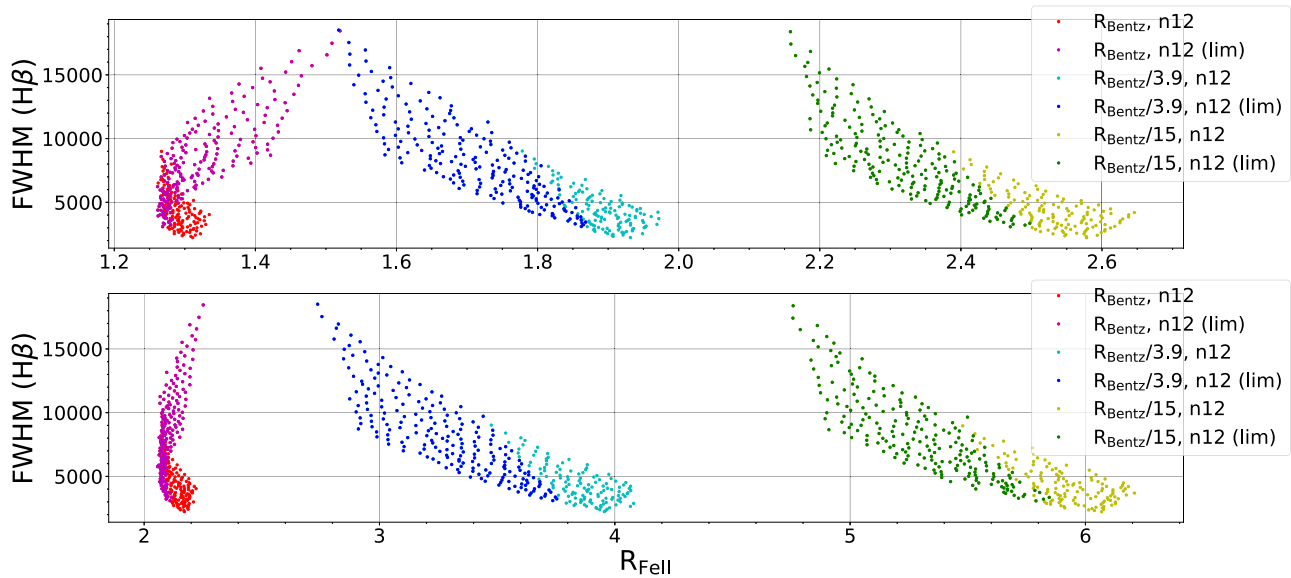


Figure 12. Fe II strength as a function of the size of the BLR. We show three cases of changing BLR sizes: at R_{Bentz} (Bentz et al. 2013), and at two other sizes scaled with respect to R_{Bentz} (derived from the largest deviation, i.e., 15 days and its standard deviation (≈ 3.9 days) in the $\tau-\lambda L_V$ relation; Grier et al. 2017). The panels are shown for a cloud density of 10^{12} cm^{-3} at solar metallicity. The two cases are color-coded as in Figure 6. Top panel: at zero turbulence. Bottom panel: at turbulence 10 km s^{-1} . The FWHMs for the $R_{\text{Bentz}}/3.9$ and the $R_{\text{Bentz}}/15$ cases have been scaled with f factors of $\sqrt{3.9}$ and $\sqrt{15}$, respectively, to recover line widths identical to the original R_{Bentz} case.

range may be partially related to the viewing angle dependence of the line width, which is not yet included in our model.

In the same way as we modeled the optical plane, we also modeled the UV plane observationally discussed by Śniegowska et al. (2018). In this case, $H\beta$ is replaced with the Mg II line, and the optical Fe II emission with the UV Fe II emission. We performed the modeling using CLOUDY v17.01 and the entire methodology as before. The modeling was overall successful; we can recover the main trends for the following range of parameters: $\log n_{\text{H}}$ (in cm^{-3}) = 10–12, solar to 10 times solar abundances, 0–20 km s^{-1} microturbulence, for a single-density cloud at a high column density ($\log N_{\text{H}}$ (in cm^{-2}) = 24). The predicted line width was as before, because in our method we assumed the same location for $H\beta$ and Mg II, which is a good approximation.

In this model of the optical plane, we use only a single cloud density and position as a representation of the whole BLR, which we know is extended. We tested the dependence of the line luminosity on that mean radius, and we noticed a considerable rise in the relative Fe II optical luminosity. However, we cannot predict the net result of the broadening of the region because this would require an arbitrary assumption about the cloud distribution as a function of the radius, which would provide us with the relative importance of the different BLR radii.

5. Conclusions

We show that a simple model of $H\beta$ and Fe II production in the optical band, with a minimum number of free parameters, is able to reproduce the observed coverage of the optical plane by quasars from the Shen et al. (2011) catalog. The presence of the warm corona in the quasar SED is an important element, decreasing the dependence of the parameter $R_{\text{Fe II}}$ on the Eddington ratio. The full coverage of the plane requires the presence of sources with high metallicity although the central part of the quasar distribution is well recovered with solar metallicity. The UV plane is not as well reconstructed, and the

current model requires very high turbulence velocity. Further research of the UV plane coverage is clearly needed. The key parameters behind the quasar main sequence are the black hole mass, Eddington ratio, cloud density, and metallicity, with the last two quantities likely correlated to the first two.

The project was partially supported by the Polish Funding Agency National Science Centre, project 2015/17/B/ST9/03436/ (OPUS 9).

Software: CLOUDY v17.01 (Ferland et al. 2017), MATPLOTLIB (Hunter 2007).

ORCID iDs

Swayamtrupta Panda  <https://orcid.org/0000-0002-5854-7426>

Bożena Czerny  <https://orcid.org/0000-0001-5848-4333>

References

- Adhikari, T. P., Rózańska, A., Czerny, B., Hryniewicz, K., & Ferland, G. J. 2016, *ApJ*, **831**, 68
- Arnaud, K. A., Branduardi-Raymont, G., Culhane, J. L., et al. 1985, *MNRAS*, **217**, 105
- Bentz, M. C., Denney, K. D., Grier, C. J., et al. 2013, *ApJ*, **767**, 149
- Boroson, T. A. 2002, *ApJ*, **565**, 78
- Boroson, T. A., & Green, R. F. 1992, *ApJS*, **80**, 109
- Calderone, G., Nicastro, L., Ghisellini, G., et al. 2017, *MNRAS*, **472**, 4051
- Collin-Souffrin, S., Dyson, J. E., McDowell, J. C., & Perry, J. J. 1988, *MNRAS*, **232**, 539
- Czerny, B., Nikolajuk, M., Rózańska, A., et al. 2003, *A&A*, **412**, 317
- Czerny, B., Panda, S., Śniegowska, M., et al. 2018a, arXiv:1806.06741
- Czerny, B., Wang, J.-M., Du, P., et al. 2018b, *ApJ*, **870**, 84
- Du, P., Hu, C., Lu, K.-X., et al. 2014, *ApJ*, **782**, 45
- Du, P., Lu, K.-X., Zhang, Z.-X., et al. 2016a, *ApJ*, **825**, 126
- Du, P., Wang, J.-M., Hu, C., et al. 2016b, *ApJL*, **818**, L14
- Du, P., Zhang, Z.-X., Wang, K., et al. 2018, *ApJ*, **856**, 6
- Dultzin-Hacyan, D., & Ruano, C. 1996, *A&A*, **305**, 719
- Elvis, M., Wilkes, B. J., McDowell, J. C., et al. 1994, *ApJS*, **95**, 1
- Ferland, G. J., Chatzikos, M., Guzmán, F., et al. 2017, *RMxAA*, **53**, 385
- Gierliński, M., & Done, C. 2004, *MNRAS*, **349**, L7
- GRAVITY Collaboration, Sturm, E., Dexter, J., et al. 2018, *Natur*, **563**, 657

- Grier, C. J., Trump, J. R., Shen, Y., et al. 2017, *ApJ*, **851**, 21
- Hunter, J. D. 2007, *CSE*, **9**, 90
- Jin, C., Ward, M., & Done, C. 2012a, *MNRAS*, **422**, 3268
- Jin, C., Ward, M., Done, C., & Gelbord, J. 2012b, *MNRAS*, **420**, 1825
- Kovačević-Dojčinović, J., & Popović, L. Č. 2015, *ApJS*, **221**, 35
- Kubota, A., & Done, C. 2018, *MNRAS*, **480**, 1247
- Kuraszkiewicz, J., Wilkes, B. J., Schmidt, G., et al. 2009, *ApJ*, **692**, 1180
- Laor, A., Fiore, F., Elvis, M., Wilkes, B. J., & McDowell, J. C. 1997, *ApJ*, **477**, 93
- Lusso, E., & Risaliti, G. 2017, *A&A*, **602**, A79
- Magdziarz, P., Blaes, O. M., Zdziarski, A. A., Johnson, W. N., & Smith, D. A. 1998, *MNRAS*, **301**, 179
- Marin, F. 2014, *MNRAS*, **441**, 551
- Marziani, P., Dultzin, D., Sulentic, J. W., et al. 2018, *FrASS*, **5**, 6
- Marziani, P., Sulentic, J. W., Negrete, C. A., et al. 2014, *AstRv*, **9**, 6
- Mejía-Restrepo, J. E., Lira, P., Netzer, H., Trakhtenbrot, B., & Capellupo, D. M. 2018, *NatAs*, **2**, 63
- Middei, R., Bianchi, S., Cappi, M., et al. 2018, *A&A*, **615**, A163
- Middei, R., Bianchi, S., Petrucci, P.-O., et al. 2019, *MNRAS*, **483**, 4695
- Netzer, H. 2015, *ARA&A*, **53**, 365
- Novikov, I. D., & Thorne, K. S. 1973, in *Black Holes*, ed. C. Dewitt & B. S. Dewitt (New York: Gordon and Breach), 343
- Padovani, P., Alexander, D. M., Assef, R. J., et al. 2017, *A&ARv*, **25**, 2
- Panda, S., Czerny, B., Adhikari, T. P., et al. 2018a, *ApJ*, **866**, 115
- Panda, S., Małek, K., Śniegowska, M., & Czerny, B. 2018b, arXiv:1804.09954
- Petrucci, P.-O., Paltani, S., Malzac, J., et al. 2013, *A&A*, **549**, A73
- Petrucci, P.-O., Ursini, F., De Rosa, A., et al. 2018, *A&A*, **611**, A59
- Porquet, D., Reeves, J. N., Matt, G., et al. 2018, *A&A*, **609**, A42
- Porquet, D., Reeves, J. N., O'Brien, P., & Brinkmann, W. 2004, *A&A*, **422**, 85
- Richards, G. T., Lacy, M., Storrie-Lombardi, L. J., et al. 2006, *ApJS*, **166**, 470
- Shen, Y., & Ho, L. C. 2014, *Natur*, **513**, 210
- Shen, Y., Richards, G. T., Strauss, M. A., et al. 2011, *ApJS*, **194**, 45
- Śniegowska, M., Kozłowski, S., Czerny, B., & Panda, S. 2018, arXiv:1810.09363
- Sulentic, J. W., Zwitter, T., Marziani, P., & Dultzin-Hacyan, D. 2000, *ApJL*, **536**, L5
- Sun, M., Xue, Y., Wang, J., Cai, Z., & Guo, H. 2018, *ApJ*, **866**, 74
- Vestergaard, M., & Wilkes, B. J. 2001, *ApJS*, **134**, 1
- Wang, J.-G., Dong, X.-B., Wang, T.-G., et al. 2009, *ApJ*, **707**, 1334